Electronic Supplementary Material (ESI) for Physical Chemistry Chemical Physics.
This journal is © the Owner Societies 2023

Electronic Supplementary Information for

Tunable multiple nonvolatile resistance states in MnSe-based van der Waals multiferroic tunnel junction

Xiao-hui Guo, Lin Zhu *, Zeng-Lin Cao, and Kai-Lun Yao

School of Physics and Wuhan National High Magnetic field center, Huazhong University of Science and Technology,

Wuhan 430074, People's Republic of China

Author to whom correspondence should be addressed: linzh@hust.edu.cn

Section I. Calculation details for determination of U

To better describe the strong electron correlation effects of Mn atom, it needs to consider the GGA+U method.[1] In order to determine an appropriate U value, we have tested the optimized lattice constants of MnSe with different U values from 1 to 5 eV, as listed in Table S1. At U_{eff} = 2.3 eV, the optimized lattice constants of MnSe monolayer (a = b = 4.28 Å) are the same as the experimental values (a = b = 4.28 Å).[2] Then we explore the influence of U values on the relative energy difference between the four magnetic configurations: ferromagnetic (FM), Neel antiferromagnetic (Neel-AFM), Zigzag antiferromagnetic (Zigzag-AFM) and Stripy antiferromagnetic (Stripy-AFM) spin configurations, all the results show that the Neel-AFM configuration is the most stable phase. Previous work has provided that U=2.3 eV can better improve the lattice constants and magnetic properties of MnSe, and the hexagonal phase of MnSe was more stable.[2,3] Thus the U_{eff} =2.3 eV is taken for the 3d electron of the Mn atom in our work, which is in line with previous work.[2,3]

Table S1 The optimized lattice constants a and b (Å), energy difference ΔE per unit cell (in meV/u.c.) for four different magnetic configurations of MnSe monolayer with different effective U values. Here, the energy of the Neel-AFM is set to zero and the experimental data are bracketed to compare.

U_{eff} (eV)	a, b (Å)	FM	Neel-AFM	Zigzag-AFM	Stripy-AFM
0	4.106	742	0	248	26
0.5	4.163	599	0	212	31
1.0	4.204	537	0	197	33
1.5	4.236	484	0	183	35
2.0	4.264	437	0	171	36
2.1	4.269	428	0	169	36
2.2	4.273	420	0	166	36
2.3	**4.280 (4.28)**	**412**	**0**	**164**	**36**
2.4	4.283	404	0	162	36
2.5	4.289	396	0	160	37
2.6	4.291	388	0	157	37
2.7	4.294	381	0	156	37
2.8	4.296	373	0	154	37
2.9	4.302	367	0	152	37
3.0	4.306	360	0	150	37
3.5	4.324	328	0	140	37
4.0	4.339	300	0	132	37
4.5	4.351	273	0	124	37
5.0	4.364	250	0	117	37

Section II. The influence of exchange-correlation functionals

In order to determine the effect of the exchange correlation (XC) functions on the results, we have carried out some tests. Firstly, the influence of XC functionals on the ground state magnetic configuration of MnSe is investigated by selecting the PBE[4], RPBE[5], PW91[6] and PBEsol[7] functionals. As listed in Table S2, all the results indicate that the Neel-AFM configuration is most stable, which is consistent with the experimental results.[2] Secondly, the impact of the XC functionals on device optimization is investigated. All the device optimizations are still performed by the Atomistix ToolKit package. As shown in Table S3, the optimized left interface distance (d_L) and right interface distance (d_R) of MnSe-Fe_3GeTe_2 heterojunction in the device are almost invariant with different XC functions. Finally, the band structure of MnSe, Cu electrode and Fe_3GeTe_2 electrode is calculated with different XC functionals, as shown in Fig. S1, Fig. S2 and Fig. S3, respectively. It is evident that the band structures are almost the same for different XC functionals (PBE, RPBE, PW91, PBEsol). The PBE calculation underestimates the band gap of the semiconductor in general, so we calculate the band structure of MnSe monolayer using the HSE06 hybrid functional (see Fig. S1(e)).[8] Although the band gap calculated by HSE06 is larger (3.02 eV), the transport properties should be similar to those calculated by PBE, except for certain numerical differences. Therefore, the results are almost insensitive to the XC functionals.

Table S2 Energy difference ΔE per unit cell (in meV/u.c.) for four different magnetic configurations of MnSe monolayer calculated by different exchange-correlation functionals. Here, the energy of the Neel-AFM is set to zero.

Magnetic type	FM	Neel-AFM	Zigzag-AFM	Stripy-AFM
ΔE (meV/u.c.) [PBE]	412	0	164	36
ΔE (meV/u.c.) [RPBE]	396	0	163	39
ΔE (meV/u.c.) [PW91]	408	0	156	29
ΔE (meV/u.c.) [PBEsol]	404	0	164	38

Table S3 The left and right MnSe-Fe_3GeTe_2 interface distances (d_L and d_R) for Fe_3GeTe_2/AB-stacking MnSe/Fe_3GeTe_2 device with different XC functionals.

	PBE	RPBE	PW91	PBEsol
d_L (Å)	2.52	2.524	2.517	2.518
d_R (Å)	2.54	2.549	2.542	2.551

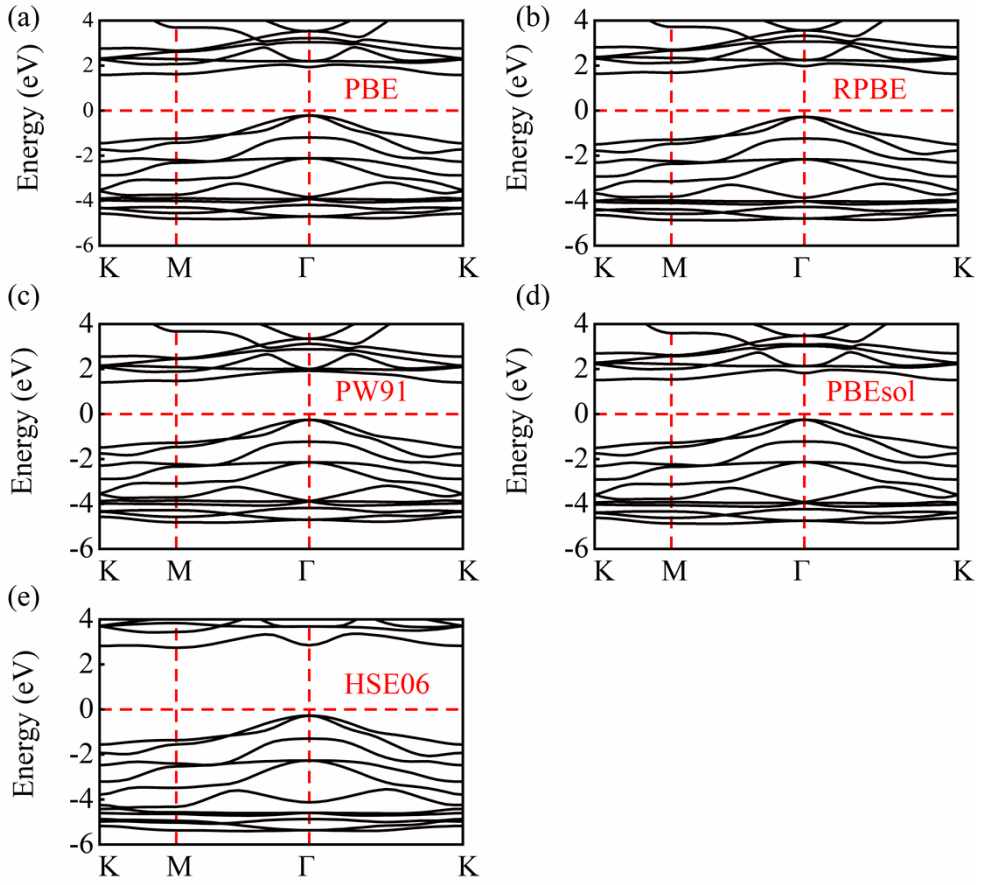

Fig. S1 The calculated band structure of MnSe monolayer with different XC functionals: (a) PBE functional, (b) RPBE functional, (c) PW91 functional, (d) PBEsol functional and (e) HSE06 functional.

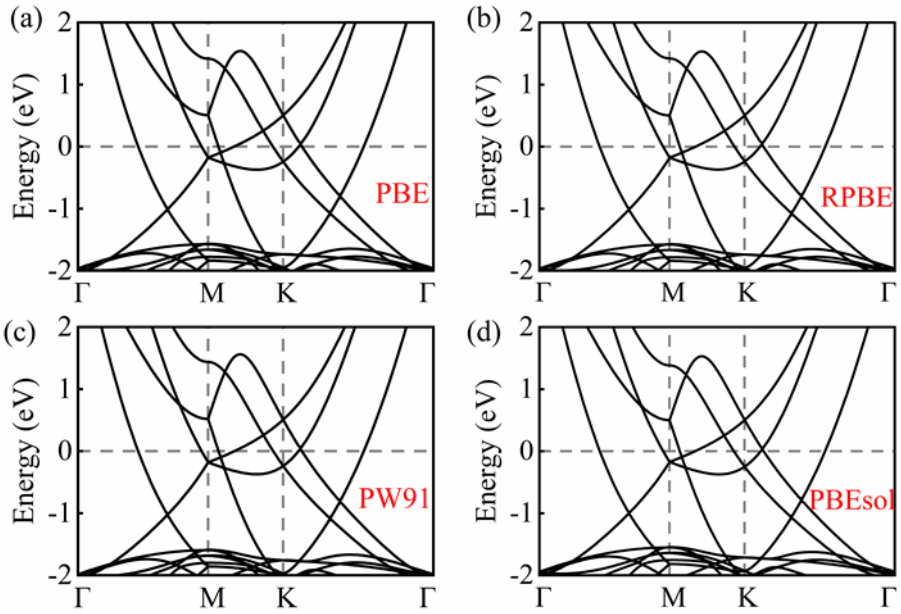

Fig. S2 The calculated band structure of Cu electrode with different XC functionals: (a) PBE functional, (b) RPBE functional, (c) PW91 functional and (d) PBEsol functional.

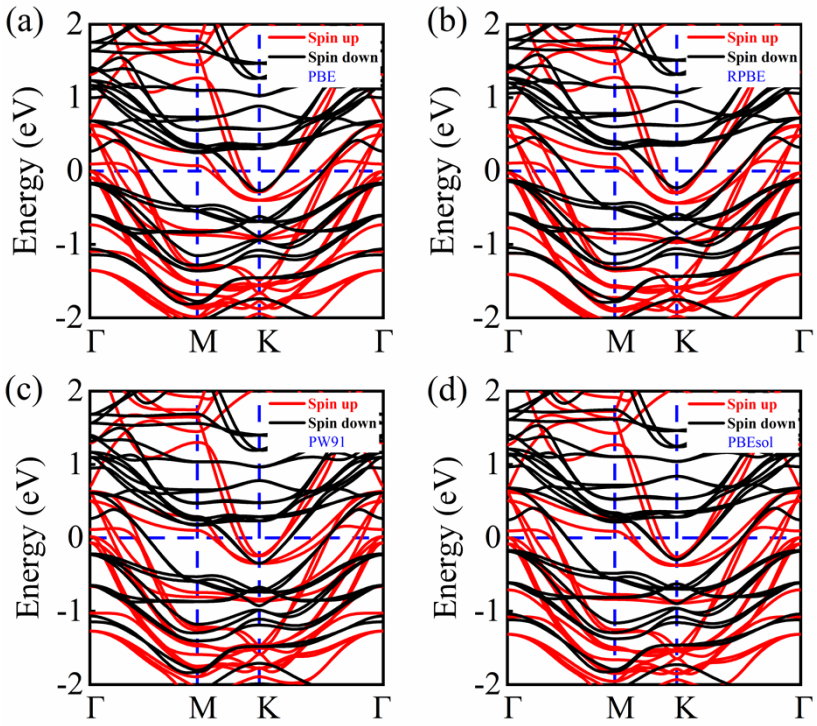

Fig. S3 The calculated band structure of Fe_3GeTe_2 electrode with different XC functionals: (a) PBE functional, (b) RPBE functional, (c) PW91 functional and (d) PBEsol functional.

Section III. Sliding ferroelectricity in MnSe bilayer and multilayers

The MnSe bilayer belongs to space group 156 ($P3m1$) and the interlayer distance between the two MnSe monolayers along the out-of-plane direction is 2.8 Å. The staggered stacking MnSe bilayer exhibit sliding ferroelectricity and the corresponding bi-stable structures are displayed in Fig. S4(a). It is clear that for state I (denoted as AB), the Mn atoms of the top layer are directly above the Se atoms of the bottom layer, while the Mn atoms of the bottom layer are located directly below the center of the upper hexagon, with the polarization direction pointing upwards. For state II (denoted as BA), the polarization direction pointing downwards. The calculated vertical spontaneous polarization of the MnSe bilayer is 3.30 pC m^{-1}. The NEB method can estimate the transition path between AB and BA, which are connected by the intermediate transition state (TS). As shown in Fig. S4(b), the energy barrier of polarization reversal is 8.35 meV per formula, which is significantly lower than that of In_2Se_3 (about 66 meV per formula),[9] and is comparable to that of BN (about 4 meV per formula).[10] The small transition barrier implies the availability of ferroelectric switching at environmental conditions. Furthermore, the spontaneous polarization can be attributed to a net charge transfer between the top and bottom sublayers, which further leads to an interface dipole and electrostatic potential step ΔV across the interface.[11,12] Fig. S4(c-h) show the plane averaged differential charge density, the three-dimensional charge density difference and the plane averaged electrostatic potential of MnSe bilayer in AB, TS and BA stacking configurations. It can be observed that in the intermediate transition state (TS), there is no potential step ΔV. However, in the ferroelectric AB and BA stacking, the charge transfer direction is opposite and the energy is discontinuity between the vacuum levels of the top and bottom sublayers, which corresponds to an electrostatic potential difference of ΔV = 0.237 eV for the AB state and ΔV= -0.237 eV for the BA state.

Similarly, the spontaneous polarization of the trilayer and tetralayer MnSe are calculated to be 8.86 pC m^{-1} and 13.25 pC m^{-1}, respectively, which are both larger than that of the MnSe bilayer. For trilayer MnSe, the stacking order of the two polarization states is denoted as ABA and BAB (Fig. S5(a)). The electric polarization direction can be switched by sliding the middle sublayer relative to the top and bottom sublayers, and there is an observed polarization reversal barrier of 11.29 meV per formula (Fig. S5(b)). For tetralayer MnSe, the stacking order of two different polarization states is denoted as ABAB and BABA (Fig.S6(a)). The orientation of electric polarization can be reversed by sliding the second and fourth sublayers, and the polarization reversal barrier is 12.31 meV per formula (Fig. S6(b)), which is still lower than that of In_2Se_3 (about 66 meV per formula).[9] In addition, we also plot the plane-averaged differential charge density, three-dimensional charge density difference and the plane averaged electrostatic potential of trilayer and tetralayer MnSe in different stacking sequences, as shown in Fig. S5(c-h) and Fig. S6(c-h). The electrostatic potential step of the trilayer MnSe is observed to be 0.47 eV, while that of tetralayer MnSe is 0.72 eV.

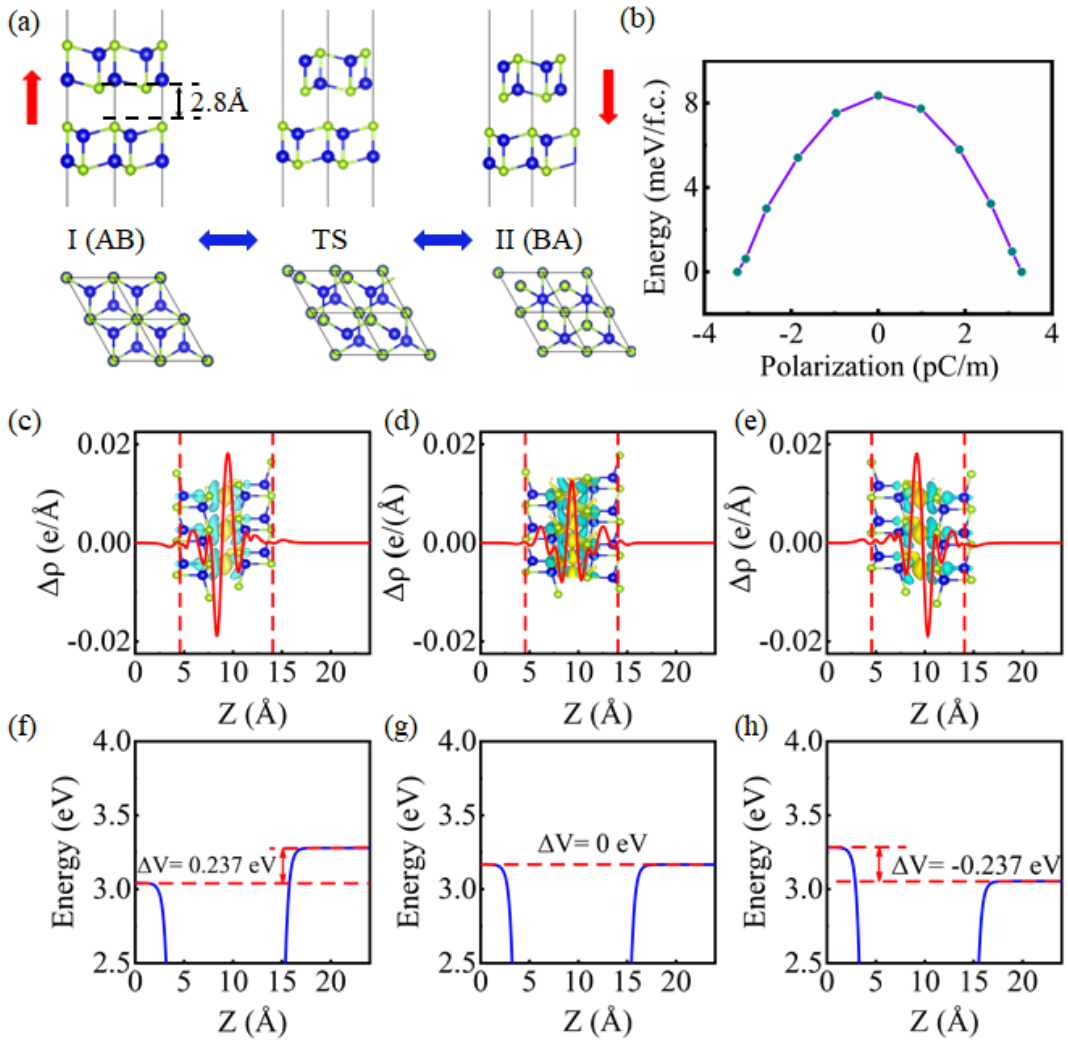

Fig. S4 (a) Top and side views of the atomic configuration of MnSe bilayer (AB, TS, BA). I and II represent two equivalent states, where the polarization directions are indicated by red arrows. (b) Energy potential barriers vs polarization for MnSe bilayer. (c)-(e) Plane-averaged differential charge density and three-dimensional charge density difference for AB, TS and BA stacking patterns of the MnSe bilayer. The yellow and green areas indicate electron accumulation and depletion, respectively, and the isosurface value is 1.49×10^{-5} /Å^3. (f)-(h) Plane averaged electrostatic potentials of MnSe bilayer in AB, TS, BA stacking configurations along the z directions.

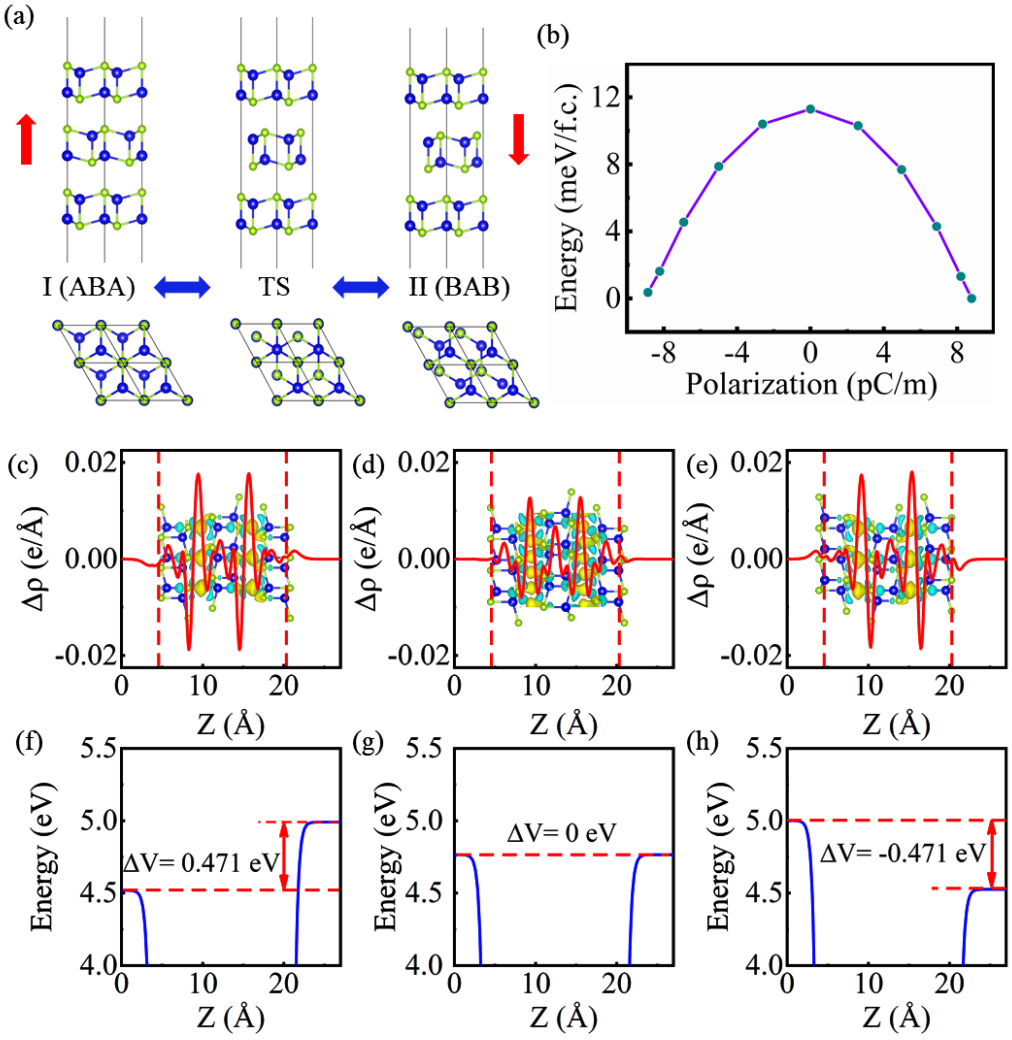

Fig. S5 (a) Top and side views of the atomic configuration of trilayer MnSe (ABA, TS, BAB). I and II represent two equivalent states, where the polarization directions are indicated by red arrows. (b) Energy potential barriers vs polarization for trilayer MnSe. (c)-(e) Plane-averaged differential charge density and three-dimensional charge density difference for ABA, TS and BAB stacking patterns of the trilayer MnSe. The yellow and green areas indicate electron accumulation and depletion, respectively, and the isosurface value is 2.08×10^{-5} e/Å^3. (f)-(h) Plane averaged electrostatic potentials of trilayer MnSe in ABA, TS, BAB stacking configurations along the z directions.

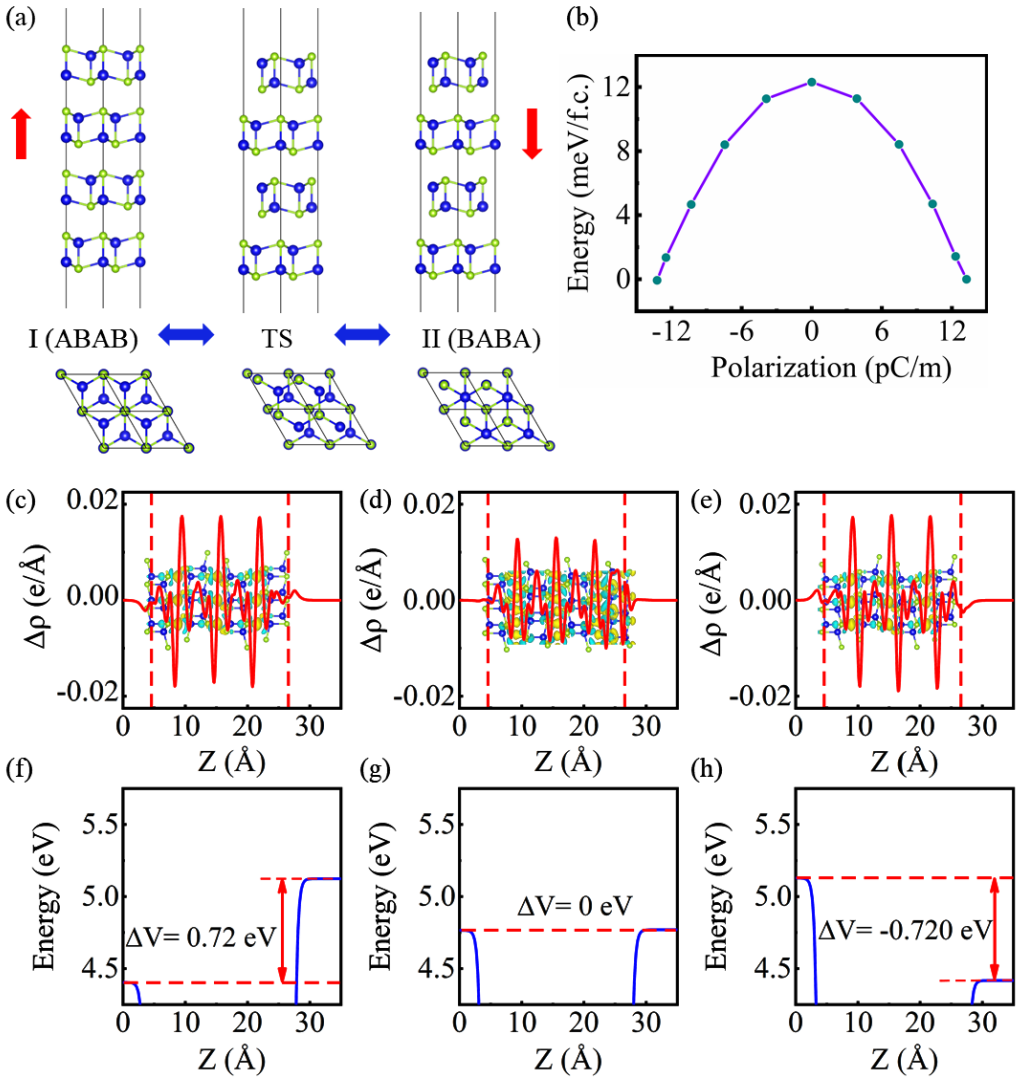

Fig. S6 (a) Top and side views of the atomic configuration of tetralayer MnSe (ABAB, TS, BABA). I and II represent two equivalent states, where the polarization directions are indicated by red arrows. (b) Energy potential barriers vs polarization for tetralayer MnSe. (c)-(e) Plane-averaged differential charge density and three-dimensional charge density difference for ABAB, TS and BABA stacking patterns of the tetralayer MnSe. The yellow and green areas indicate electron accumulation and depletion, respectively, and the isosurface value is 2.21×10^{-5} e/Å^3. (f)-(h) Plane averaged electrostatic potentials of tetralayer MnSe in ABAB, TS, BABA stacking configurations along the z directions.

Section IV. The effect of vdW corrections on the optimized interface distances

In our work, the devices consisting of MnSe barrier and Fe_3GeTe_2 electrodes are optimized using the Atomistix ToolKit package. In order to investigate the effect of different types of vdW functional on the distance between MnSe and Fe_3GeTe_2, we have chosen Grimme DFT-D2 [13] and DFT-D3 [14]. As listed in Table S4, when Grimme DFT-D3 (DFT-D2) method is used to calculate the van der Waals interaction in Fe_3GeTe_2/MnSe bilayer/Fe_3GeTe_2 MFTJ with right ferroelectric polarization of MnSe (AB-stacking), the distances between the left and right Fe_3GeTe_2-MnSe interfaces are 2.52 (2.55) Å and 2.54 (2.57) Å, respectively. In addition, when employing Grimme DFT-D3 (DFT-D2) method to calculate the van der Waals interaction of Fe_3GeTe_2/MnSe bilayer/Fe_3GeTe_2 MFTJ with left ferroelectric polarization of MnSe (BA-stacking), the distances between the left and right Fe_3GeTe_2-MnSe interfaces are 2.57 (2.61) Å and 2.12 (2.16) Å, respectively. The results reveal that the difference of the interface distance obtained by these two methods is very small. Since the influence of Grimme DFT-D3 and Grimme DFT-D2 on the interface distance is negligible, but the DFT-D3 method can better handle the weak interlayer interaction, we finally use the Grimme DFT-D3 method for van der Waals corrections in the device optimization.

Table S4 The left and right MnSe-Fe_3GeTe_2 interface distances (d_L and d_R) calculated using the Grimme DFT-D3 and Grimme DFT-D2 van der Waals correction methods.

Junctions	d_L (DFT-D2)	d_R (DFT-D2)	d_L (DFT-D3)	d_R (DFT-D3)
Fe_3GeTe_2/AB-stacking MnSe/Fe_3GeTe_2	2.55 Å	2.57 Å	2.52 Å	2.54 Å
Fe_3GeTe_2/BA-stacking MnSe/Fe_3GeTe_2	2.61 Å	2.16 Å	2.57 Å	2.12 Å

Section V. Supplementary Tables and Figures

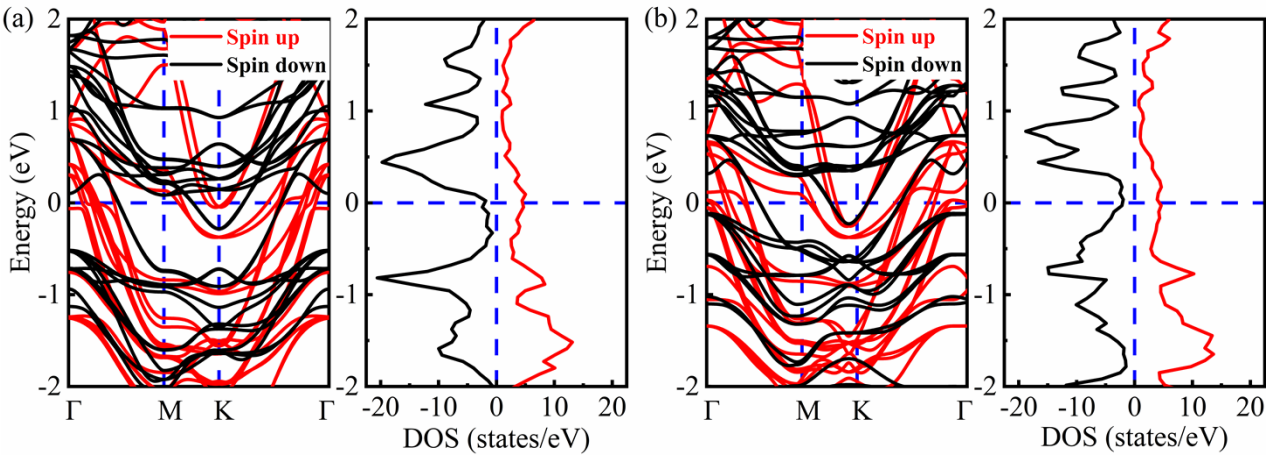

Fig. S7 The band structures and density of states for Fe_3GeTe_2 bulk at 0% (a) and 5.6% (b) strain.

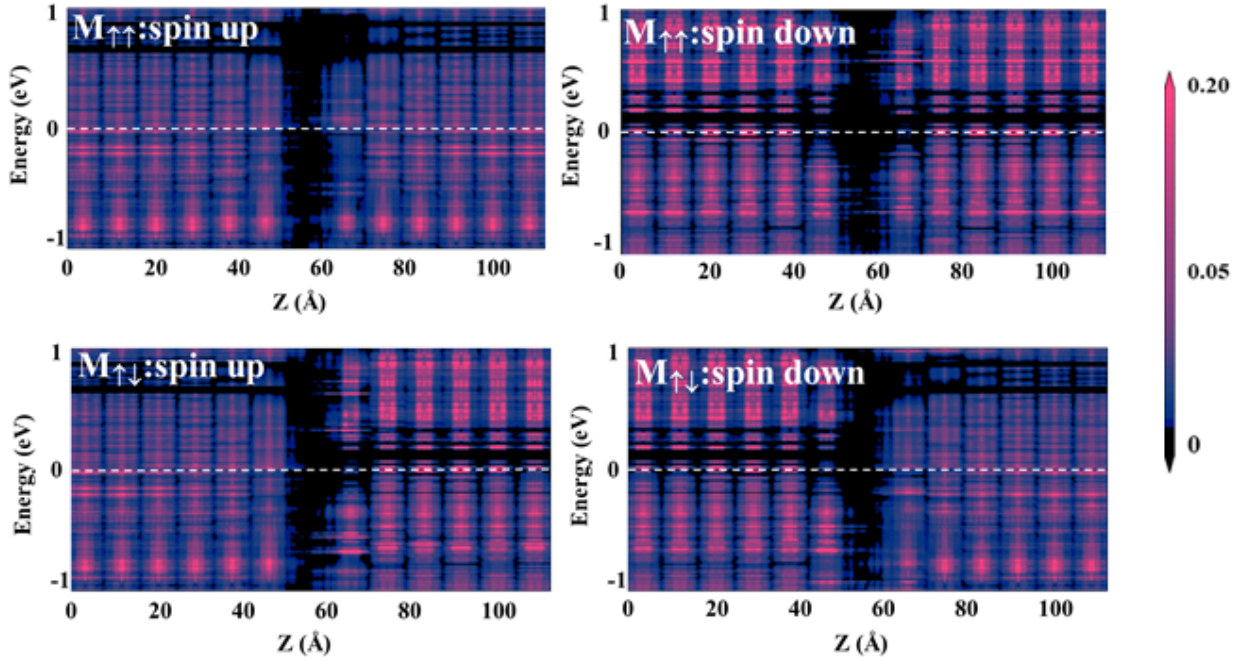

Fig. S8 Spin-dependent projected local density of states of Fe_3GeTe_2/MnSe bilayer/Fe_3GeTe_2 MFTJs for $P_{\leftarrow}$ (BA-stacking) state. Here, the dashed white line represents the Fermi level.

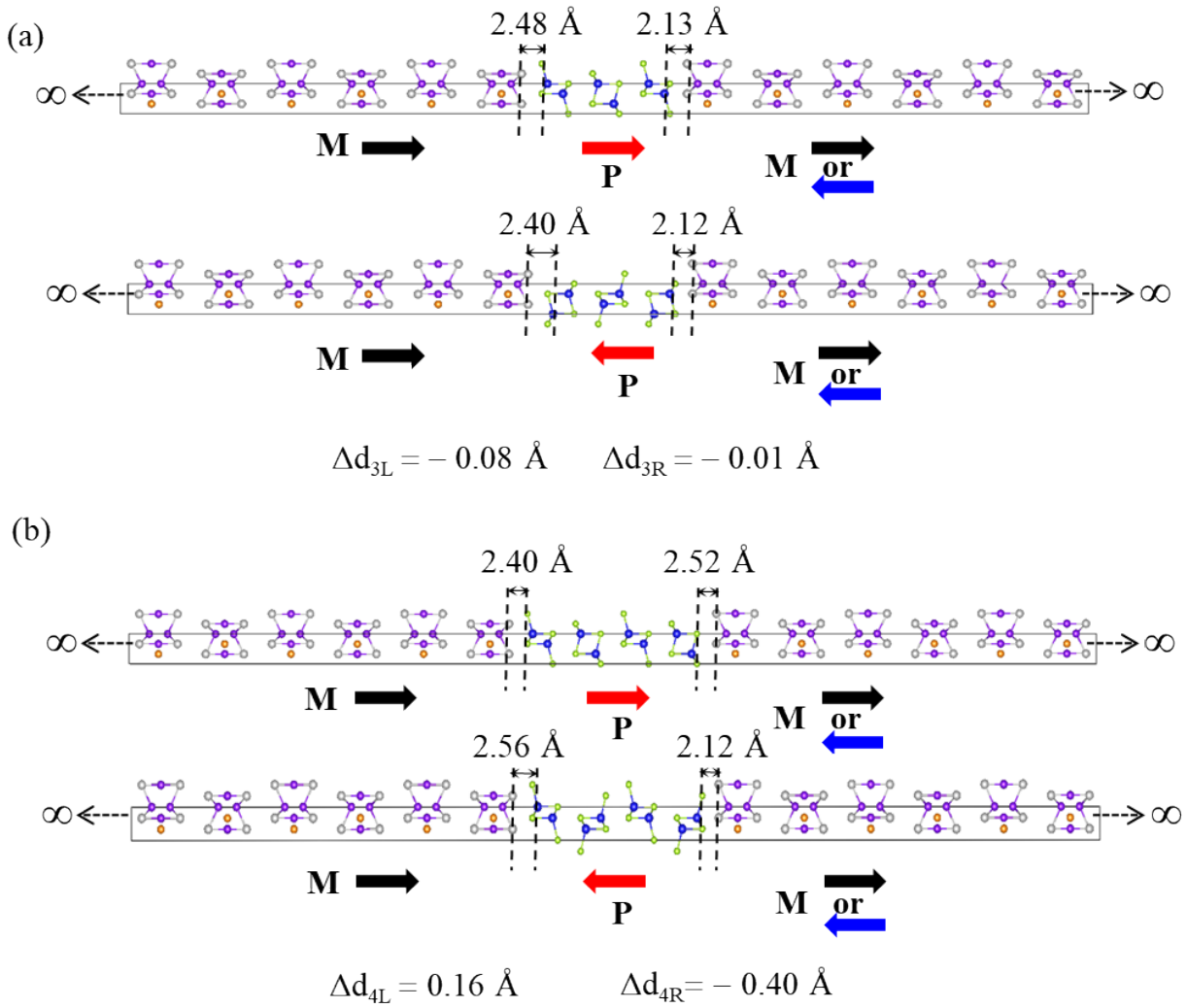

Fig. S9 Device configuration of MnSe trilayer (a) and MnSe tetralayer (b) with different atomic arrangements sandwiched between Fe_3GeTe_2 semi-infinite electrodes, where the polarization directions are indicated by red arrows, while the magnetization directions are represented by the black arrows or blue arrows.

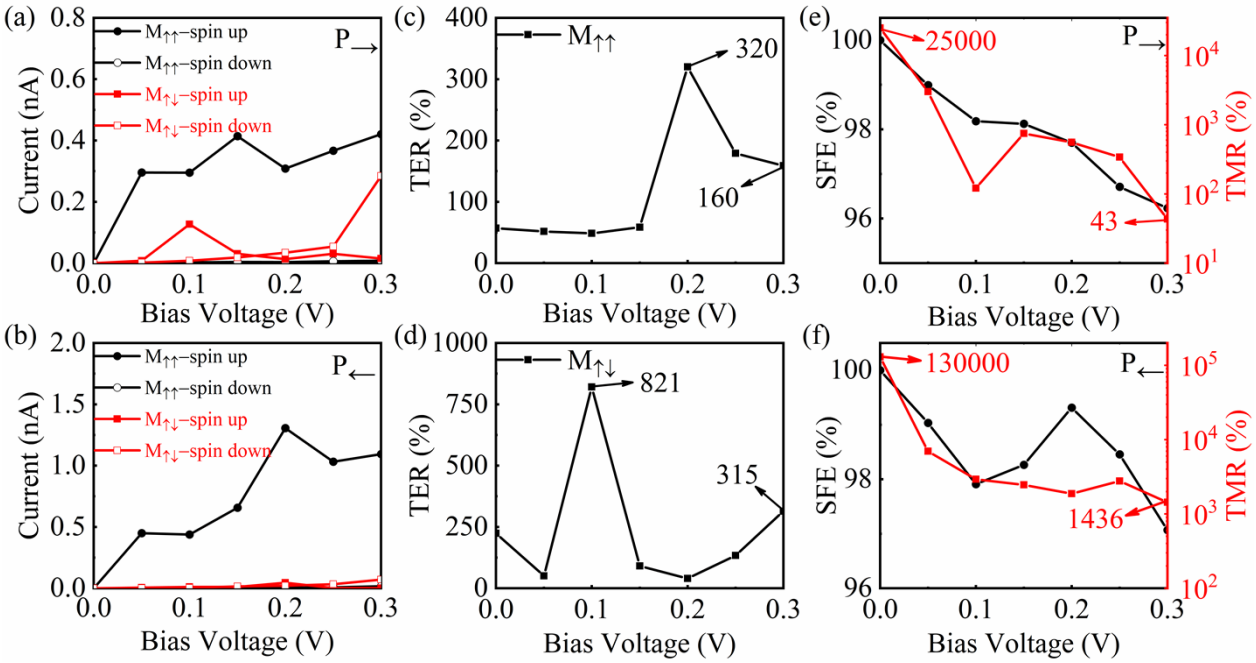

Fig. S10 The spin current of the $M_{\uparrow\uparrow}$ and $M_{\uparrow\downarrow}$ magnetization alignment for ABA-stacking ($P_{\rightarrow}$) (a) and BAB-stacking ($P_{\leftarrow}$) (b). The TER for $M_{\uparrow\uparrow}$ (c) and $M_{\uparrow\downarrow}$ (d) state. The TMR ratios and spin filtering effect η with the bias voltages for Fe_3GeTe_2/3L-MnSe/Fe_3GeTe_2 MFTJs in different polarized states: (e) $P_{\rightarrow}$ state, (f) $P_{\leftarrow}$ state.

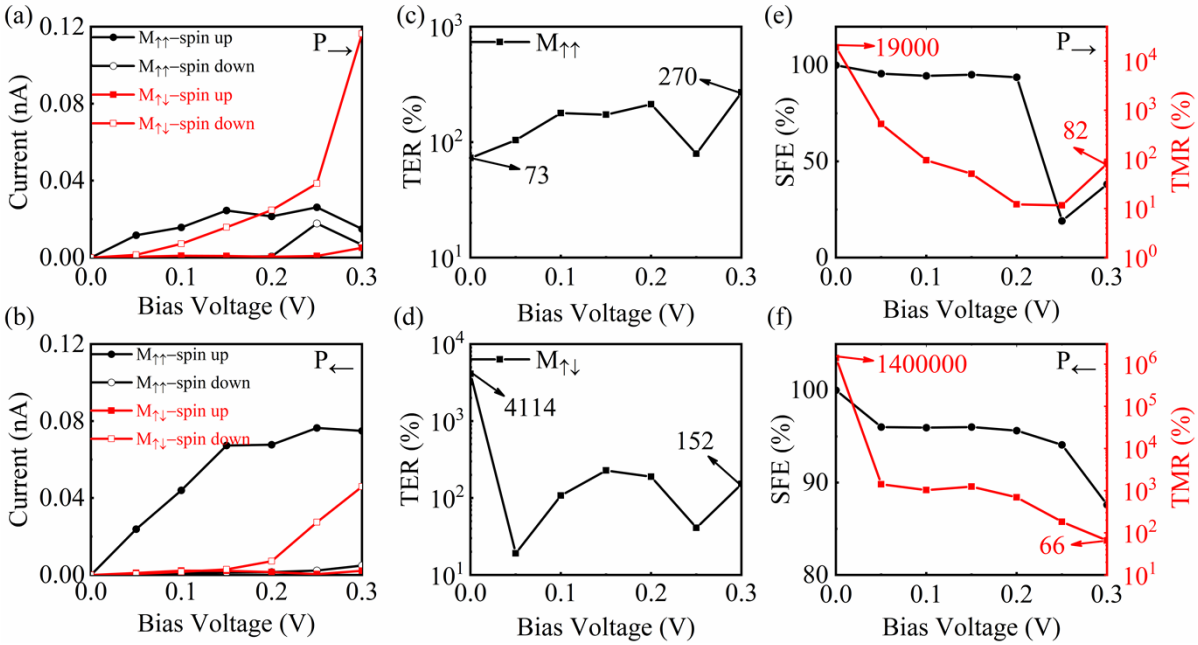

Fig. S11 The spin current of the $M_{\uparrow\uparrow}$ and $M_{\uparrow\downarrow}$ magnetization alignment for ABAB-stacking ($P_{\rightarrow}$) (a) and BABA-stacking ($P_{\leftarrow}$) (b). The TER ratios for $M_{\uparrow\uparrow}$ (c) and $M_{\uparrow\downarrow}$ (d) states. The TMR ratios and spin filtering effect η with the bias voltages for Fe_3GeTe_2/4L-MnSe/Fe_3GeTe_2 MFTJs in different polarized states. (e) $P_{\rightarrow}$ state, (f) $P_{\leftarrow}$ state.

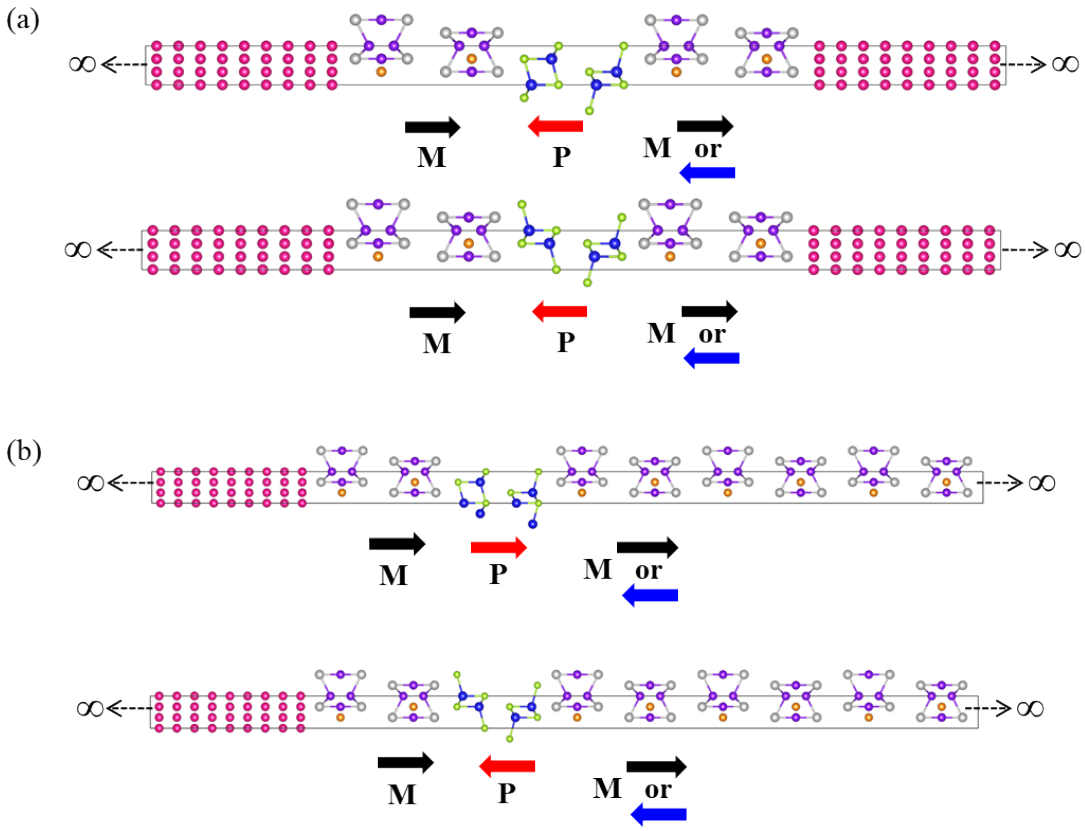

Fig. S12 Device configuration of Cu/Fe_3GeTe_2/2L-MnSe/Fe_3GeTe_2/Cu (a) and Cu/Fe_3GeTe_2/2L-MnSe/Fe_3GeTe_2 (b), where the polarization directions are indicated by red arrows, while the magnetization directions are represented by the black arrows or blue arrows.

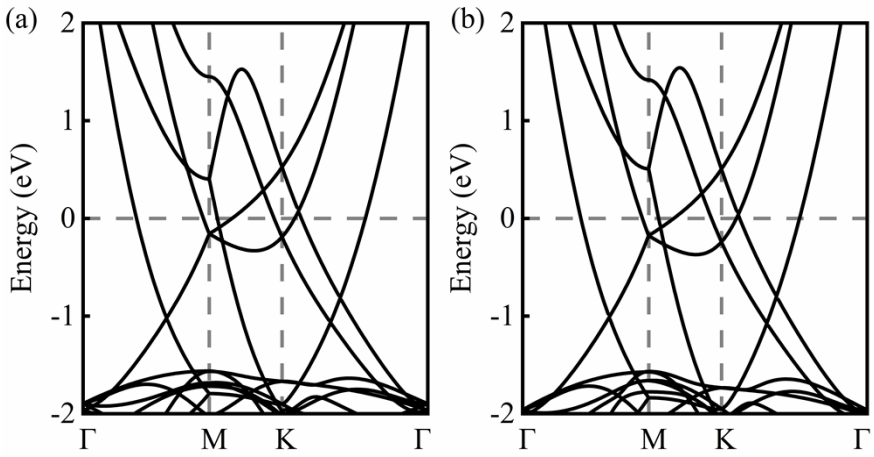

Fig. S13 The band structures for Cu electrode at 0% (a) and 3.1% (b) strain.

Table S5 Spin-dependent electron transmission $T_{\uparrow}$ and $T_{\downarrow}$, TMR, TER and spin filtering efficiency η for $Cu/Fe_3GeTe_2/2L\text{-}MnSe/Fe_3GeTe_2/Cu$ MFTJs at zero bias voltage.

	$M_{\uparrow\uparrow}$ (parallel magnetization)				$M_{\uparrow\downarrow}$ (antiparallel magnetization)				
	$T_{\uparrow}$	$T_{\downarrow}$	$T(=T_{\uparrow}+T_{\downarrow})$	η	$T_{\uparrow}$	$T_{\downarrow}$	$T(=T_{\uparrow}+T_{\downarrow})$	η	TMR
$p_{\rightarrow}$	1.3×10^{-3}	4.4×10^{-7}	$\sim 1.3 \times 10^{-3}$	~ 100%	3.0×10^{-4}	9.6×10^{-5}	$\sim 4.0 \times 10^{-4}$	~ 51%	225%
$P_{\leftarrow}$	8.4×10^{-3}	3.4×10^{-5}	$\sim 8.4 \times 10^{-3}$	~ 100%	1.9×10^{-4}	1.5×10^{-4}	$\sim 3.4 \times 10^{-4}$	~ 12%	2370%
TER	546%				18%				

Table S6 Spin-dependent electron transmission $T_{\uparrow}$ and $T_{\downarrow}$, TMR, TER and spin filtering efficiency η for $Cu/Fe_3GeTe_2/2L\text{-}MnSe/Fe_3GeTe_2$ MFTJs at zero bias voltage.

	$M_{\uparrow\uparrow}$ (parallel magnetization)				$M_{\uparrow\downarrow}$ (antiparallel magnetization)				
	$T_{\uparrow}$	$T_{\downarrow}$	$T(=T_{\uparrow}+T_{\downarrow})$	η	$T_{\uparrow}$	$T_{\downarrow}$	$T(=T_{\uparrow}+T_{\downarrow})$	η	TMR
$p_{\rightarrow}$	1.1×10^{-3}	3.0×10^{-8}	$\sim 1.1 \times 10^{-3}$	~ 100%	2.7×10^{-5}	7.5×10^{-5}	$\sim 1.0 \times 10^{-4}$	~ 47%	1000%
$P_{\leftarrow}$	7.9×10^{-3}	1.8×10^{-7}	$\sim 7.9 \times 10^{-3}$	~ 100%	4.6×10^{-6}	3.0×10^{-5}	$\sim 3.5 \times 10^{-5}$	~ 73%	22471%
TER	618%				186%				

References:

1 S. L. Dudarev, G. A. Botton, S. Y. Savrasov, C. J. Humphreys and A. P. Sutton, *Phys. Rev. B*, 1998, **57**, 1505.

2 M. Aapro, M. N. Huda, J. Karthikeyan, S. Kezilebieke, S. C. Ganguli, H. G. Herrero, X. Huang, P. Liljeroth and H.-P. Komsa, *ACS Nano*, 2021, **15**, 13794-13802.

3 K. Liu, X. Ma, S. Xu, Y. Li and M. Zhao, *npj Comput. Mater.*, 2023, **9**, 16.

4 J. P. Perdew, K. Burke and M. Ernzerhof, *Phys. Rev. Lett*., 1996, **77,** 3865.

5 B. Hammer, L. B. Hansen and J. K. Nørskov, *Phys. Rev. B*, 1999, **59**, 7413.

6 J. P. Perdew, J. A. Chevary, S. H. Vosko, K. A. Jackson, M. R. Pederson, D. J. Singh, and C. Fiolhais, *Phys. Rev. B*, 1992, **46**, 6671.

7 J. P. Perdew, A. Ruzsinszky, G. I. Csonka, O. A. Vydrov, G.E. Scuseria, L. A. Constantin, X. Zhou, and K. Burke, *Phys. Rev. Lett*., 2008, **100**, 136406.

8 A. V. Krukau, O. A. Vydrov, A. F. Izmaylov and G. E. Scuseria, *J. Chem. Phys.*, 2006, **125**, 224106.

9 W. Ding, J. Zhu, Z. Wang, Y. Gao, D. Xiao, Y. Gu, Z. Zhang and W. Zhu, *Nat. Commun.*, 2017, **8**, 14956.

10 L. Li and M. Wu, *ACS Nano*, 2017, **11**, 6382-6388.

11 Z. Lin, C. Si, S. Duan, C. Wang and W. Duan, *Phys. Rev. B*, 2019, **100**, 155408.

12 C. Si, Z. Lin, J. Zhou and Z. Sun, *2D Mater*, 2017, **4**, 015027.

13 S. Grimme, *J. Comput. Chem.*, 2006, **27**, 1787-1799.

14 S. Grimme, J. Antony, S. Ehrlich and H. Krieg, *J. Chem. Phys.*, 2010, **132**, 154104.